REPORT DOCUMENTATION PAGE

Form Approved OMB NO. 0704-0188

1. REPORT DATE (DD-MM-YYYY)	2. REPORT TYPE	3. DATES COVERED (From - To)
10-02-2016	Final Report	20-Jul-2012 - 19-Oct-2015

4. TITLE AND SUBTITLE
Final Report: First Principles Modeling of Structure and Transport in Solid Polymer Electrolytes, Ionic Liquids, and Methanol/Water Mixtures

5a. CONTRACT NUMBER
W911NF-12-1-0320

5b. GRANT NUMBER

5c. PROGRAM ELEMENT NUMBER
611102

6. AUTHORS
Stephen J Paddison

5d. PROJECT NUMBER

5e. TASK NUMBER

5f. WORK UNIT NUMBER

7. PERFORMING ORGANIZATION NAMES AND ADDRESSES
University of Tennessee at Knoxville
Office of Sponsored Programs
1534 White Avenue
Knoxville, TN 37996 -1529

8. PERFORMING ORGANIZATION REPORT NUMBER

9. SPONSORING/MONITORING AGENCY NAME(S) AND ADDRESS (ES)
U.S. Army Research Office
P.O. Box 12211
Research Triangle Park, NC 27709-2211

10. SPONSOR/MONITOR'S ACRONYM(S)
ARO

11. SPONSOR/MONITOR'S REPORT NUMBER(S)
60020-CH.8

12. DISTRIBUTION AVAILIBILITY STATEMENT
Approved for Public Release; Distribution Unlimited

13. SUPPLEMENTARY NOTES
The views, opinions and/or findings contained in this report are those of the author(s) and should not contrued as an official Department of the Army position, policy or decision, unless so designated by other documentation.

14. ABSTRACT
We have undertaken simulations and calculations on three distinct systems: (1) polyethylene oxide-alkali salts systems with the general formula: PEO6:XPF6, where X = H, Li, or Na; (2) methanol/water solution over a range of methanol mole fractions (0 to 1); and (3) electrolytes for magnesium batteries incorporating chloro- or iodo- ionic liquids. Much of this work was done in collaboration with the experimental group of Prof. Vito Di Noto at the University of Padua, Italy. We have sought to understand structure/function relationships using first principles based methods including ab initio molecular dynamics simulations and density functional theory based electronic

15. SUBJECT TERMS
ab initio molecular dynamics, quantum chemistry, electronic structure, solid polymer electrolytes, ionic liquids, methanol/water mixtures

16. SECURITY CLASSIFICATION OF:			17. LIMITATION OF ABSTRACT	15. NUMBER OF PAGES	19a. NAME OF RESPONSIBLE PERSON
a. REPORT	b. ABSTRACT	c. THIS PAGE			Stephen Paddison
UU	UU	UU	UU		19b. TELEPHONE NUMBER 865-974-2026

Report Title

Final Report: First Principles Modeling of Structure and Transport in Solid Polymer Electrolytes, Ionic Liquids, and Methanol/Water Mixtures

ABSTRACT

We have undertaken simulations and calculations on three distinct systems: (1) polyethylene oxide-alkali salts systems with the general formula: PEO6:XPF6, where X = H, Li, or Na; (2) methanol/water solution over a range of methanol mole fractions (0 to 1); and (3) electrolytes for magnesium batteries incorporating chloro- or iodo- ionic liquids. Much of this work was done in collaboration with the experimental group of Prof. Vito Di Noto at the University of Padua, Italy. We have sought to understand structure/function relationships using first principles based methods including ab initio molecular dynamics simulations and density functional theory based electronic structure calculations. Specifically, in crystalline PEO6:XPF6 systems we confirmed that the dynamics of the chains play an important role in the diffusion mechanism and computed diffusion barriers for H+, Li+, and Na+. In our AIMD simulations of the water-methanol mixtures we determined that at low methanol concentrations the water forms percolating hydrogen bond networks. When a moderate electric field was applied a "hollow channel" was observed in the methanol-rich mixtures. Finally, in our quantum chemical calculations of the magnesium battery electrolytes we were able to make all vibrational frequency assignments (measured in the IR and Raman spectra) and confirm the overall concatenated structure of the ionic liquids in the amorphous delta-Mg chloride/iodide.

Enter List of papers submitted or published that acknowledge ARO support from the start of the project to the date of this printing. List the papers, including journal references, in the following categories:

(a) Papers published in peer-reviewed journals (N/A for none)

Received		Paper
08/30/2013	1.00	Aniruddha Deb, Y. Sakurai, M. Itou, V. G. Krishnan, S. J. Paddison, G. F. Reiter. Anomalous Ground State of the Electrons in Nanoconfined Water, Physical Review Letters, (07 2013): 36803. doi: 10.1103/PhysRevLett.111.036803
TOTAL:	**1**	

Number of Papers published in peer-reviewed journals:

(b) Papers published in non-peer-reviewed journals (N/A for none)

Received		Paper
TOTAL:		

Number of Papers published in non peer-reviewed journals:

(c) Presentations

Number of Presentations: 6.00

Non Peer-Reviewed Conference Proceeding publications (other than abstracts):

Received	Paper

TOTAL:

Number of Non Peer-Reviewed Conference Proceeding publications (other than abstracts):

Peer-Reviewed Conference Proceeding publications (other than abstracts):

Received	Paper

TOTAL:

Number of Peer-Reviewed Conference Proceeding publications (other than abstracts):

(d) Manuscripts

Received	Paper	
08/29/2014	2.00	Jun He, Stephen J. Paddison. Structural relaxation and cation (H+, Li+, Na+) diffusion in crystallinepolymer electrolytes: Ab initio molecular dynamics simulations, Chemical Physics Letters (09 2014)
08/29/2014	3.00	Federico Bertasi, Chaminda Hettige, Fatemeh Sepehr, Xavier Bogle, Gioele Pagot, Keti Vezzù, Enrico Negro, Stephen J. Paddison, Steve G. Greenbaum, Michele Vittadello, Vito Di Noto. A Key Concept in Magnesium Secondary Battery Electrolytes: 3DChloride-Concatenated Dynamic Ionic Liquid Networks, Nature Nanotechnology (submitted) (07 2014)
TOTAL:	**2**	

Number of Manuscripts:

Books

Received Book

TOTAL:

Received Book Chapter

TOTAL:

Patents Submitted

Patents Awarded

Awards

Royal Academy of Engineering Distinguished Visiting Fellowship 6/2015
Visiting Scientist, Department of Chemical Sciences, University of Padova, Padova, Italy 7/2015

Graduate Students

NAME	PERCENT_SUPPORTED	Discipline
Fatemeh Sepehr	0.10	
FTE Equivalent:	**0.10**	
Total Number:	**1**	

Names of Post Doctorates

NAME	PERCENT_SUPPORTED
Jun He	1.00
FTE Equivalent:	**1.00**
Total Number:	**1**

Names of Faculty Supported

NAME	PERCENT_SUPPORTED	National Academy Member
Stephen J. Paddison	0.10	
FTE Equivalent:	**0.10**	
Total Number:	**1**	

Names of Under Graduate students supported

NAME	PERCENT_SUPPORTED
FTE Equivalent:	
Total Number:	

Student Metrics

This section only applies to graduating undergraduates supported by this agreement in this reporting period

The number of undergraduates funded by this agreement who graduated during this period: 0.00

The number of undergraduates funded by this agreement who graduated during this period with a degree in science, mathematics, engineering, or technology fields:..... 0.00

The number of undergraduates funded by your agreement who graduated during this period and will continue to pursue a graduate or Ph.D. degree in science, mathematics, engineering, or technology fields:..... 0.00

Number of graduating undergraduates who achieved a 3.5 GPA to 4.0 (4.0 max scale):..... 0.00

Number of graduating undergraduates funded by a DoD funded Center of Excellence grant for Education, Research and Engineering:..... 0.00

The number of undergraduates funded by your agreement who graduated during this period and intend to work for the Department of Defense 0.00

The number of undergraduates funded by your agreement who graduated during this period and will receive scholarships or fellowships for further studies in science, mathematics, engineering or technology fields: 0.00

Names of Personnel receiving masters degrees

NAME
Total Number:

Names of personnel receiving PHDs

NAME
Total Number:

Names of other research staff

NAME	PERCENT_SUPPORTED
FTE Equivalent:	
Total Number:	

Sub Contractors (DD882)

Inventions (DD882)

Scientific Progress

See attachment and uploaded reprints and manuscripts.

Technology Transfer

Final Report: 60020-CH

Described below are the three projects we have worked on during the duration of this funded project.

Project I: Structural Relaxation and Cation (Li^+, H^+, Na^+) Diffusion in Crystalline Polymer Electrolytes

Note: See attached manuscript (to be submitted to *Chemical Physics Letters)* for complete details of this work.

Crystalline polymer electrolytes represent a class of new materials which have great potential in making high-performance solid state lithium ion batteries [1,2]. Among them, the polyethylene oxide-alkali salts systems PEO_6:XPF_6 (X = H, Li, Na) are of particular interest. Although the ionic conductivity found in PEO_6:XPF_6 systems are an order of magnitude higher than that in its equivalent amorphous materials, it is still too low for industrial applications [3,4]. The transport mechanisms are not well understood.

We have investigated the structural stability and transport behavior of crystalline PEO_6:XPF_6 (X = H, Li, Na) systems at 300K used *ab initio* molecular dynamics (AIMD) simulations. Both the pristine and defective structures were studied. Simulations of the electronic structure DFT calculation were performed using the projector augmented-wave method (PAW) and a plane wave basis set at gamma-point as implemented in the Vienna ab initio simulation package (VASP) code [5,6]. During the molecular dynamics simulations, the supercells were heated to 300K via repeated velocity rescaling for 1 ps; and then equilibrated at 300K in an NVT (canonical) ensemble for 5 ps with a time step of 0.5 fs. In the production runs, the supercell was equilibrated at 300 K in a NVT (canonical) ensemble for 15 ps.

1. Structural stability of pristine PEO systems

We reconfirmed that the chain dynamics is crucial to the ion conducting in both pristine and defective PEO systems. For PEO_6:$LiPF_6$, the Li-O bond distances predicted in by our simulations at 0 K show both 4-fold and 5-fold Li-O coordination. The previous experimental study by Gadjurova et al. [7] only observed 5-fold Li-O coordination. This discrepancy is due to the considerable movement of the PF_6^- anions. Such movement increases the Li-P coordination and decreases the Li-O coordination, forcing the Li-O interaction into a metastable coordination. **(Figure 1)** The subtle change in coordination numbers affects the chain structure considerably. As a result, the PEO chain becomes disordered and not well aligned in the axial direction. Thus, we suggest that the interaction between the cation (H^+, Li^+, Na^+) and the anion group (PF_6^-) is crucial to the stabilization of the PEO chains and will facilitate fast cation transport inside the PEO coiled chains.

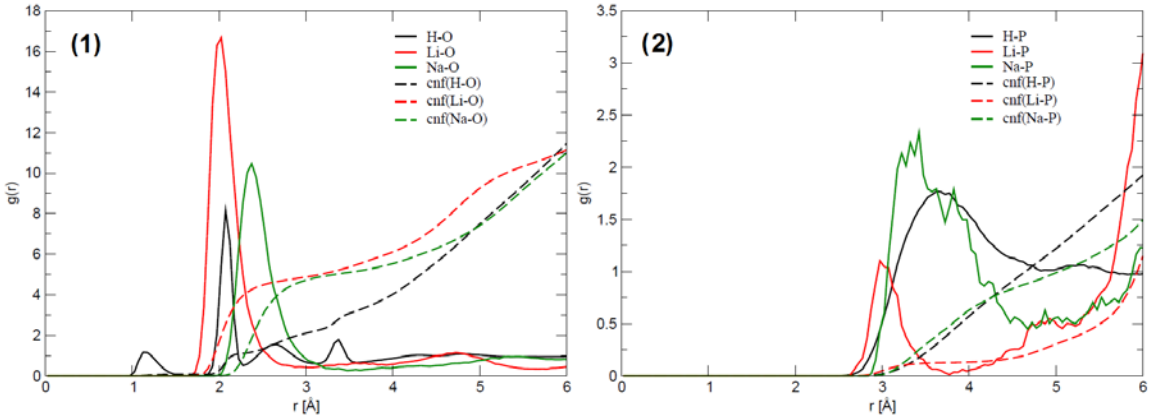

Figure 1. Radial distribution function of cation-oxygen (1), and cation-P (2) in relaxed crystalline PEO_6:HPF_6, PEO_6:$LiPF_6$ (b), and PEO_6:$NaPF_6$ at 300 K. The integrated total number of oxygen atoms around a cation and phosphorus atoms around a cation as function of separation distance is shown in dash lines.

2. Effects of cation defects on the stability of the PEO systems

Our AIMD simulations of cation defects are performed under two different scenarios: cation interstitials and cation vacancies. It was hypothesized that the effect of the introduced cation defect would be limited by the interaction between the cation (H^+, Li^+, Na^+) and the anion group (PF_6^-), and thus would have a weak effect on cation transport. Other structural aspects, including end group modification, would need to be taken into consideration to enhance the mechanical strength of the PEO chains.

3. Single cation diffusion in three PEO systems

Our diffusion analysis revealed that the Li in the PEO_6:$LiPF_6$ system has a relatively small diffusion barrier (1.20 eV) when comparing with other two studied systems (proton in PEO_6:HPF_6: 3.44 eV, Na in PEO_6:$NaPF_6$: 1.95 eV). (**Figure 2**) These barriers are expected to be smaller when an electric field is applied and this hypothesis is currently being examined.

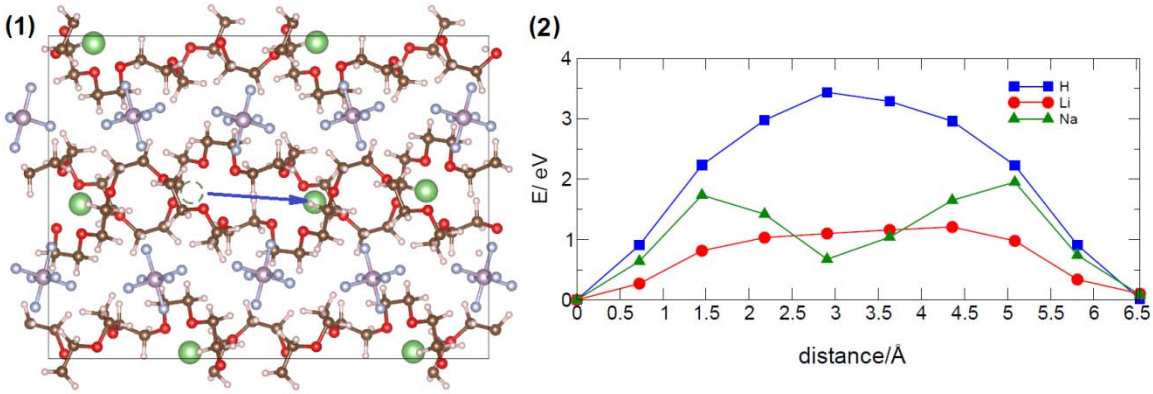

Figure 2. Cation diffusion pathway (1) in crystalline PEO_6:$LiPF_6$ and calculated diffusion energy profiles for three PEO systems (2).

Project II: The Effects of an Electric Field on the Structure of Water-Methanol Mixtures

This work is in collaboration with the experimental group of V. Di Noto, U. of Padua. The results of our extensive first principles based simulations was published in *Chemical Physics Letters,* see attached file for complete details of this work. A second manuscript described the dielectric spectroscopy results and thermodynamic analysis will be submitted to *Physical Chemistry Chemical Physics* and is also attached to this report.

Liquid water and methanol are two model molecules which show high proton conductivity due to their hydrogen bonded network. Although the methanol can be mixed with water in any arbitrary ratio, it is well known that the mixing is incomplete at the molecular level [8-11]. This can be attributed to the fact that the hydrogen bonding in liquid methanol is distinctly different from that in liquid water, owing to the presence of the hydrophobic methyl group in methanol. The application of an electric field to water-methanol mixture may result in even more complicated scenarios. Early X-ray scattering studies of pure water suggested that the water molecules are reoriented with the H-bond networks being disrupted at the surface under an electric field of 10^9 V/m, while the H-bond networks in pure methanol is enhanced under an electric field of 10^{10} V/m. Thus it is important to obtain a detailed microstructural analysis of water–methanol mixtures under ambient conditions, including both internal and external electric fields.

We have performed AIMD simulations for pure water, pure methanol, and water-methanol mixtures, the latter at different mole fractions of methanol. We have further performed simulations by applying intrinsic and extrinsic electric field to these molecular systems to study the effect of electric field on the hydrogen bonded networks. Our AIMD simulations in the canonical ensemble (NVT) were performed with the VASP code. Both pure methanol and water molecules are placed in periodic tetragonal supercell to reproduce their experimental density (methanol: 0.79 g/cm^3, water: 1.00 g/cm^3). The electronic structure DFT calculations were performed using the projector augmented-wave method (PAW) and a plane wave basis set at gamma-point. In the molecular dynamics calculation, the supercell was heated up to 300 K via repeated velocity rescaling for 1ps at a time step of 0.5 fs. Then the supercell was being equilibrated at 300 K in a NVT (canonical) ensemble for 5 ps with the same time step. In the production run, the supercell was further equilibrated at 300K in a NVT (canonical) ensemble for 15 ps. Simulations of the water-methanol mixtures were performed at six methanol mole fractions: X_M = 0.00, 0.20, 0.40, 0.60, 0.80, 1.00. The intrinsic electric field ranges from 0.0 to 1.0 V/Å at an interval of 0.25 V/Å (1.0 V/Å equals to $1x10^{10}$ V/m).

1. <u>Origin of incomplete mixing of water-methanol mixtures</u>

At low methanol concentration (X_M = 0.20) the water molecules form a percolated network surrounding short methanol chains **(Figure 3** left panel**)**, which is consistent with previous theoretical and experimental studies [11,12]. On the other hand, at high methanol concentration (X_M = 0.80), water and methanol molecules are segregated and form two separate hydrogen bond networks. (**Figure 3** middle panel) This is due to the amphiphilic characteristics of CH_3OH. Methanol has both a hydrophilic hydroxyl group and a hydrophobic alkyl group. When at low methanol concentration, hydroxyl group is dominating and therefore promotes the good solubility of methanol in water. However, at high methanol concentrations, the interaction/aggregation of the alkyl groups appears to dominate,

preferring a segregated hydrogen bond network structure for methanol. This is also confirmed by the smoothed first peak in the carbon-carbon RDFs when X_M is increased from 0.20 to 1.00 (**Figure 3** right panel).

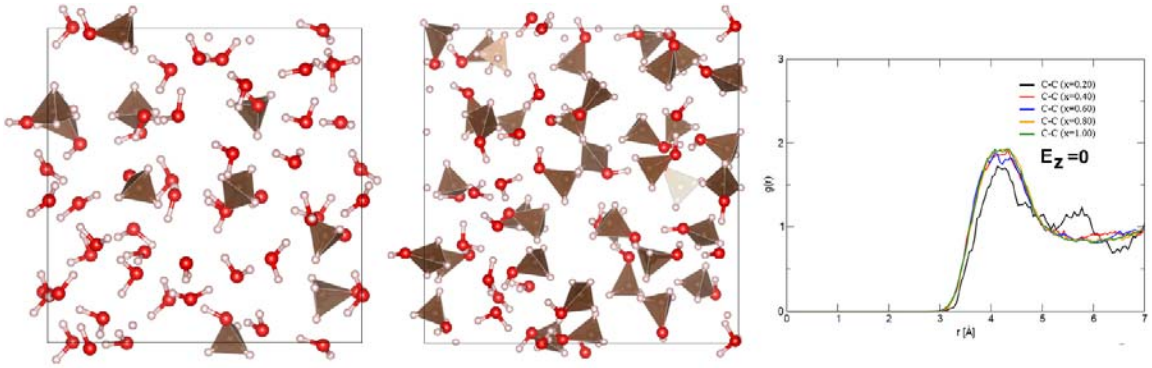

Figure 3. Snapshots of the simulation box containing the water-methanol mixtures (left panel: $X_M = 0.20$, middle panel: $X_M = 0.80$) at 300K without an electric field; and the C–C radial distribution functions as a function of the methanol mole fraction (right panel). Oxygen atoms are represented by red spheres, hydrogen atoms by white spheres, and the CH_3OH molecules with a polyhedron.

2. Effect of electric field on hydrogen bonded network in pure water and methanol

When an intrinsic electric field is applied to the water and methanol mixtures, we expect these two molecules to show a dissimilar response due to the different dipole moments and configuration. Our results show that the hydrogen bonded network in water remains in a uniform tetrahedral coordination when subject to an electric field ($0 < E < 0.75$ V/Å); when the field reaches 1.00 V/Å, about 8% of the water molecules begin to dissociate and form hydrogen molecules (H_2) and hydroxyl group pairs in the water. The presence of hydroxyl group pairs is shown as a small peak around 1.5 Å in the O–O RDFs in **Figure 4** (left panel).

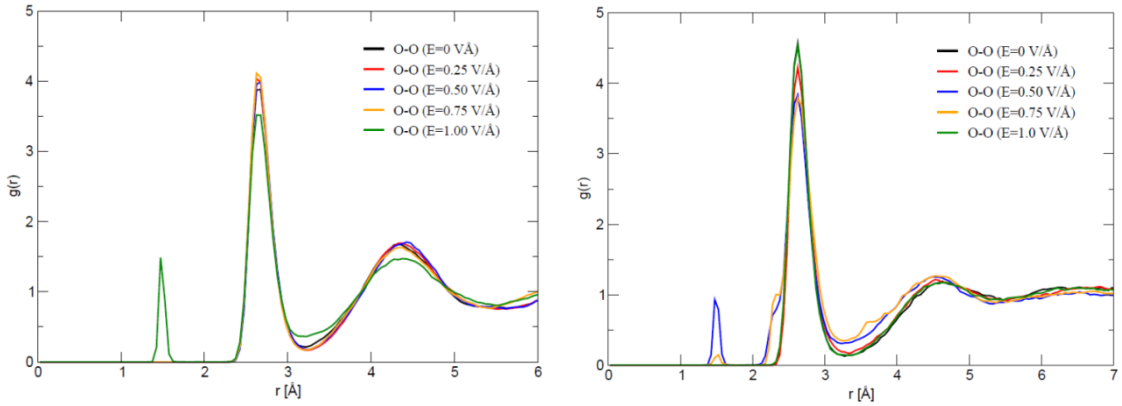

Figure 4. Radial distribution functions of the intermolecular oxygen-oxygen in liquid pure water (left) and pure methanol (right) at 300K under different electric field strengths (E ranges from 0.0 to 1.00 V/Å).

Pure methanol shows more complicated behavior when responds to the applying intrinsic electric field. When the field reaches 0.50 V/Å, about 25% of methanol molecules begin to dissociate and form hydrogen molecules, hydroxyl group, and other byproducts of small molecules (shown in small peaks around 1.5 Å and shoulders around 2.2 Å in the O–O RDFs in **Figure 4** (right panel)). When the field is at 0.75 V/Å, about 45% of the CH_3OH molecules begin to dissociate. But when the field reaches 1.00 V/Å, none of the methanol molecules appear to be dissociated. This phenomenon needs to be further investigated in future work.

3. Effect of intrinsic electric field on hydrogen bonded network in water-methanol mixtures

For the water-methanol mixtures, the effect of intrinsic electric field is complicate. At low methanol concentration ($X_M = 0.20$), the water molecules become dissociated and form hydrogen molecules and hydroxyl group pairs when the electric field reaches 0.75 V/Å and above (**Figure 5** left panel). However, water molecules still form a percolated network which is surrounding short methanol chains.

At high methanol concentration ($X_M = 0.80$), when electric field is applied, the segregation between water and methanol molecules disappears and they form uniform hydrogen bonded network. The methanol molecules also align their orientation when under the low to medium strength field (E = 0.25~0.50 V/Å). When the electric field reaches 1.00 V/Å, 10% methanol molecules begin to dissociate (**Figure 5** right panel).

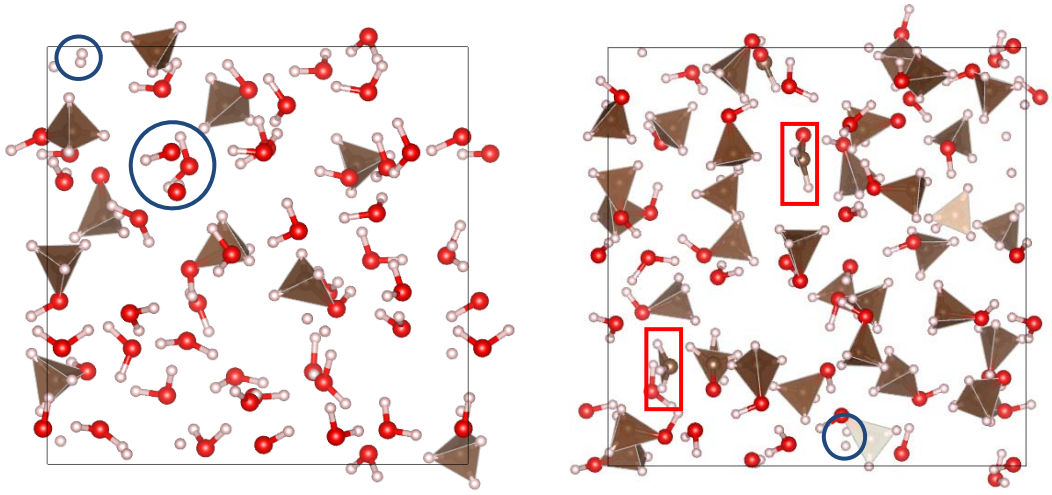

Figure 5. Snapshots taken from the simulation of the water-methanol mixtures under an electric field. Left panel: $X_M = 0.20$; E = 0.75 V/Å, the hydrogen molecules and hydroxyl group pairs are highlighted by blue circles; right panel: $X_M = 0.80$; E = 1.00 V/Å, the hydrogen molecules are indicated by blue circles, and the generated small molecules in red rectangles.

We have also calculated the hydrogen bond number in these mixtures and the results are shown in **Table 1**. When no electric field is applied, the predicted hydrogen bond numbers for both pure water and methanol from our simulations (3.96 and 2.02 H-bonds/molecule) are very consistent with the ideal values and about 6–8% higher than previous theoretical results (3.65 for water and 1.91 for methanol [13]). When an electric field is applied, it becomes clear that the hydrogen bond numbers exhibit limited enhancement when subjected to a field.

Table 1. Calculated average hydrogen bond number in water-methanol mixtures as functions of methanol mole fraction (X_M) and electric field strength (E) at 300K.

Electric field (V/ Å)	X_M=0.00 (water)	X_M=0.20	X_M=0.40	X_M=0.60	X_M=0.80	X_M=1.00 (methanol)
E=0.00	3.96	3.55	3.22	2.78	2.43	2.02
E=0.25	3.99	3.57	3.16	2.75	2.43	1.99
E=0.50	4.01	3.58	3.14	2.80	2.41	2.05
E=0.75	4.00	3.55	3.15	2.74	2.41	2.11
E=1.00	3.88	3.55	3.17	2.80	2.43	2.01

4. Hollow channel stimulated by intrinsic electric field in water-methanol mixtures

The above results indicate a limited enhancement in hydrogen bond numbers upon application of the electric field. Thus there may be some other mechanisms playing a significant role for fast proton transport in water–methanol mixtures when under electric field. We further examined the microstructure of water–methanol mixtures.

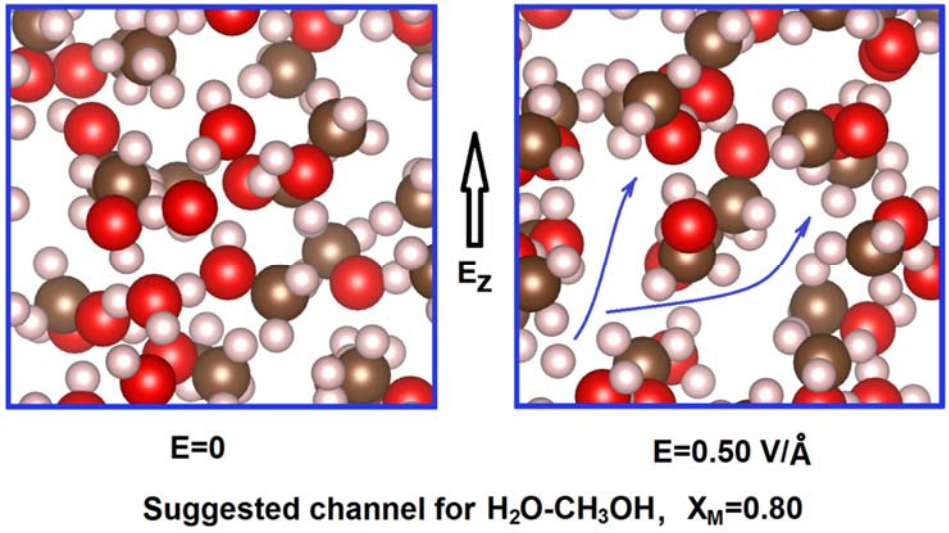

Figure 6. Snapshots of the structures of water-methanol mixture (X_M = 0.80) under two different intrinsic electric fields. Left panel: E = 0 V/Å; right panel: E = 0.50 V/Å, the blue arrows indicate the formed possible diffusion channel.

When under zero field, the water and methanol molecules in the mixture (X_M= 0.80) are segregated, forming two separate hydrogen bond networks. No sign of any long range hollow channels. When an electric field of E = 0.25 V/Å is applied, molecules aligns along the field direction, and "hollow spaces" are enlarged. When the electric field reaches a moderate strength (0.50 V/ Å), these enlarged hollow spaces begin to connect with each other (**Figure 6**

right panel). Thus long hollow channels are formed along field direction. We suggest that, these dynamical hollow structures may explain the reported abnormalities in thermo-physical properties of water–methanol mixtures.

5. Effect of extrinsic electric field on the water-methanol mixtures

Our AIMD simulations on the effect of an intrinsic electric field are with stoichiometric water-methanol systems. We are currently adding point defects (such as neutral hydrogen ion, charged proton) into the water-methanol mixtures and applying an electric field. This will simulate the effect of extrinsic electric field. Generally, intrinsic electric field intensities in condensed-matter systems are much larger than those applied externally. For example, for pure water, the intrinsic field intensity has been estimated to be in the range of ~1.5 to 2.5 V/Å, while the extrinsic field intensities are up to ~0.03-0.05 V/Å. This part of the study is still ongoing.

References

[1] P.G. Bruce, Solid State Electrolytes, Cambridge University Press, Cambridge, 1995.
[2] F. M. Gray, Polymer Electrolytes, The Royal Society of Chemistry, Cambridge, 1997.
[3] Y.G.A. Graham, S. MacGlashan, Peter G. Bruce, Structure of the polymer electrolyte poly(ethylene oxide)$_6$:LiAsF$_6$, *Nature* **398**, 792-794 (1999).
[4] P.V. Wright, Y. Zheng, D. Bhatt, T. Richardson, G. Ungar, Supramolecular order in new polymer electrolytes. *Polym. Int.* **47**, 34-42 (1998).
[5] G. Kresse, J. Furthmuller, Efficient iterative schemes for ab initio total-energy calculations using a plane-wave basis set, *Phys. Rev. B* **54**, 11169-11186 (1996).
[6] G. Kresse, D. Joubert, From ultrasoft pseudopotentials to the projector augmented-wave method, *Phys. Rev. B* **59**, 1758-1775 (1999).
[7] Z. Gadjourova, D.M. Marero, K.H. Andersen, Y.G. Andreev, P.G. Bruce, Structures of the Polymer Electrolyte Complexes PEO$_6$:LiXF$_6$ (X = P, Sb), Determined from Neutron Powder Diffraction Data, *Chem. Mater.* **13**, 1282-1285 (2001).
[8] N. Nishi, K. Koga, C. Ohshima, K. Yamamoto, U. Nagashima and K. Nagami, Molecular association in ethanol-water mixtures studied by mass spectrometric analysis of clusters generated through adiabatic expansion of liquid jets, *J. Am. Chem. Soc.*, **110**, 5246–5255 (1988).
[9] A. Wakisaka, H. Abdoul-Carime, Y. Yamamoto and Y. Kiyozumi, Non-ideality of binary mixtures Water-methanol and water-acetonitrile from the viewpoint of clustering structure, *J. Chem. Soc., Faraday Trans.,* **94**, 369–374 (1998**)**.
[10] S. Dixit, J. Crain, W. C. K. Poon, J. L. Finney and A. K. Soper, Molecular segregation observed in a concentrated alcohol–water solution, *Nature*, **416**, 829–832 (2002).
[11] I. Bakó, T. Megyes, S. Bálint, T. Grósz, and V. Chihaia, Water-methanol mixtures: topology of hydrogen bonded network, *Phys. Chem. Chem. Phys.*, **10**, 5004-5011 (2008).
[12] F. Conti, F. Romanini, and V. Di Noto, to be published (2016).
[13] M.J. McGrath, I.F.W. Kuo, J.I. Siepmann, Liquid structures of water, methanol, and hydrogen fluoride at ambient conditions from first principles molecular dynamics simulations with a dispersion corrected density functional, *Phys. Chem. Chem. Phys.*, **13**, 19943-19950 (2011).

Project III: Structures and Vibrational Frequencies of Novel Electrolytes for Magnesium Batteries (work with the experimental group of V. Di Noto, U. of Padua)

We have undertaken electronic structure calculations to determine structures and vibrational frequencies on various electrolytes for use in magnesium secondary batteries that incorporate an ionic liquid. In the first study, electrolytes based on 1-ethyl-3-methylimidazolium chloride doped with $AlCl_3$ and amorphous δ-$MgCl_2$ were investigated and the work was published and feature on the cover of *ChemSusChem* (reprint included with this report). In our second investigation we undertook a similar study with a novel iodoaluminated ionic liquid doped with AlI_3 and δ-MgI_2. A manuscript describing this work will shortly be submitted to *Journal of the American Chemical Society* - manuscript attached with this report.

EMIm/$(AlCl_3)_{1.5}$ with δ-$MgCl_2$

3D Chloride-Concatenated Dynamic Mg-ion conducting electrolytes were synthesized (by the DiNoto group) by reacting EMIm/$(AlCl_3)_{1.5}$ with δ-$MgCl_2$. The resulting systems have general formula [EMIm/$(AlCl_3)_{1.5}$]/$(\delta\text{-}MgCl_2)_x$, with molar ratio $x = n_{\delta-MgCl_2}/n_{IL}$, $0 \le x \le 0.20$, and R > 1. Four concentrations were explored ranging from pure chloroaluminate IL, EMIm/$(AlCl_3)_{1.5}$, to a saturated solution of δ-$MgCl_2$.

We performed high-level density functional theory (DFT) calculations to determine the atomic scale structures for the $EMIm^+$ cation interacting with $AlCl_4^-$, $Al_2Cl_7^-$, and $MgCl_2$. These results indicated that the anion is highly likely to occupy the forward position (position 2) around the imidazolium ring, rather than the side (1, 3) and back positions (4, 5). Adding $MgCl_2$ and $(MgCl_2)_2$ molecules to the optimized geometries revealed that the nearest anion to $EMIm^+$ is magnesium chloride rather than the aluminum chloride anions, in all cases. This is a consequence of the Mg–Cl bond being obviously more polarized than the Al–Cl bond and is confirmed by the electrostatic potential maps on electron isodensity surface of $[AlCl_4MgCl_2]^-$ and $[Al_2Cl_7MgCl_2]^-$ concatenated complexes. These maps (see **Figure 5**) show a more negative electrostatic potential and therefore more electron rich area on the magnesium bonded chloride rather than the aluminum bonded chloride. Analyzing the energetics of these systems, we determined that the binding energy of $MgCl_2$ to the $EMImAlCl_4$ structure is 5 and 7 kcal/mol lower than its binding to the $EMImAl_2Cl_7$ structure, for addition of one and two units of $MgCl_2$, respectively. This indicates that in presence of $MgCl_2$, the $AlCl_4^-$ concatenated complexes are more energetically favored compared to those based on $Al_2Cl_7^-$

complexes. However, the binding energy results were not sufficiently conclusive and so vibrational frequencies were computed and analyzed. These along with the measured IR and Raman spectra permitted assignment of all important bands (see Table 1 and 2 below).

Figure 4 Illustrated Phase Diagram of $[EMIm/(AlCl_3)_{1.5}]/(\ \delta\text{-}MgCl_2)_x$ Electrolytes. Suggested structures are partially substantiated from quantum chemical calculations

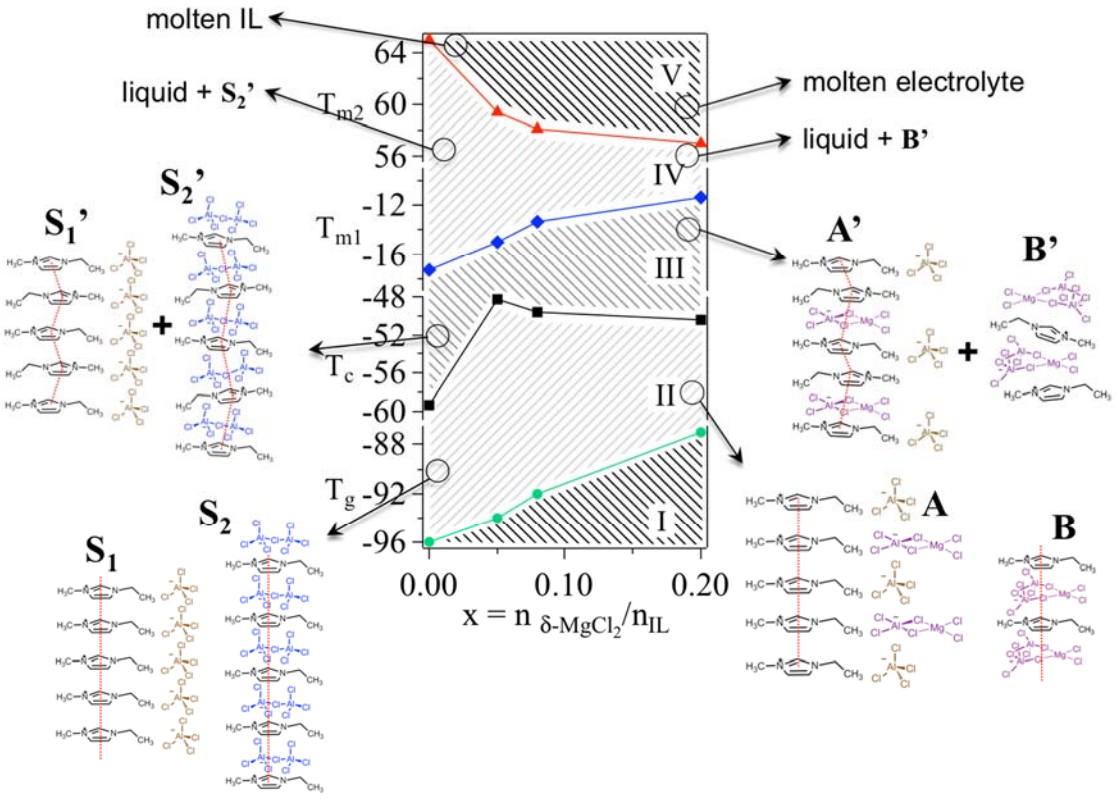

Figure 5.

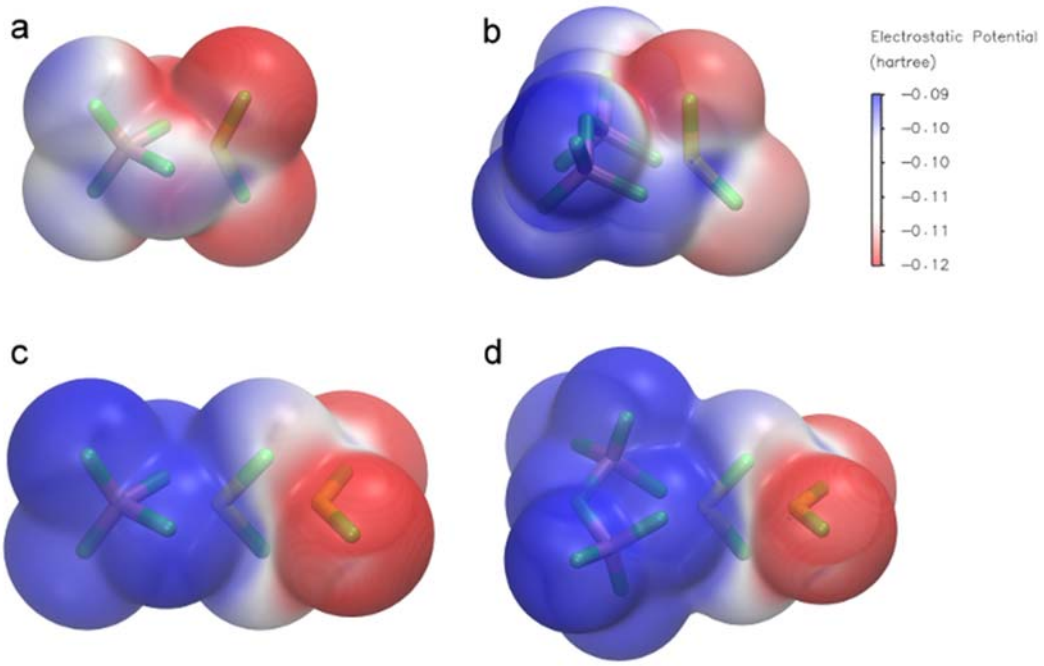

electrostatic potential maps on total electron density isosurface. **a,** $[AlCl_4MgCl_2]^-$ complex. **b,** $[Al_2Cl_7MgCl_2]^-$ complex. **c,** $[AlCl_4(MgCl_2)_2]^-$ complex. **d,** $[Al_2Cl_7(MgCl_2)_2]^-$ complex. These maps show a more negative electrostatic potential and therefore more electron rich area on magnesium bonded chloride rather than aluminum bonded chloride. Color code for atoms: chlorine, green; aluminum, pink; magnesium, yellow.

Table 1 Ab initio vibrational frequencies for $EMImAlCl_4$ and $EMImAl_2Cl_7$ in the far infrared region compared to experimental Raman and IR frequencies for $EMImCl(AlCl_3)_{1.5}$.

Structure	Calculated frequencies (cm^{-1}) at B3LYP/6-311G**	Experimental frequencies (cm^{-1})		Assignment[a]
		Raman	IR	
$AlCl_4^-$ + $EMIm^+$ ≡ Figure 2a	182	181[c], 179	180	$\delta(AlCl_4^-)$
	190			$\delta(AlCl_4^-)$
	242[b] IR inactive	241[c], 240		γ(N-Me)[d]
	350 IR inactive	350[c], 348		$\nu(AlCl_4^-)$[e]
	375[b] IR inactive	383[c], 385		γ(N-Et)
	431[b]	431		r(N-Et), r(N-Me)[d]
	477 Raman inactive			$\nu_{as}(AlCl_4^-)$
	488 Raman inactive		493	$\nu_{as}(AlCl_4^-)$
	561 Raman inactive		551	$\nu(AlCl_4^-)$
$Al_2Cl_7^-$+ $EMIm^+$ ≡ Figure 2b	156,162	157[c],156		$\delta(Al_2Cl_7^-)$
	189			$\delta(Al_2Cl_7^-)$ termin.
	241[b] IR inactive	241[c],240		γ(N-Me)[d]
	314	310[c], 311	310	$\nu_s(Al_2Cl_7^-)$ bridge
	342 weak Raman		331	$\nu_{as}(Al_2Cl_7^-)$ bridge[f]
	380[b] IR inactive	383[c], 385		γ(N-Et)
	393	383[c], 385	385	$\nu(Al_2Cl_7^-)$ termin, out of phase
	427[b]	432[c], 431		r(N-Et), r(N-Me)[d]
	448	432[c], 431	433	$\nu(Al_2Cl_7^-)$ termin., in phase
	538		536	$\nu(Al_2Cl_7^-)$ termin.
	576,586	566[c]		$\nu(Al_2Cl_7^-)$ termin.

[a] ν stretching, δ bending, r rocking, γ out of plane, s symmetrical, as antisymmetrical.

[b] Calculated frequency is not scaled.

[c] Takahashi, S. et al. Molecular orbital calculations and Raman measurements for 1-ethyl-3-methylimidazolium chloroaluminates. *Inorganic Chemistry* **34**, 2990-2993 (1995).

[d] Katsyuba, S. A. et al. Application of density functional theory and vibrational spectroscopy toward the rational design of ionic liquids. *J. Phys. Chem. A* **111**, 352-370 (2007).

[e] Nakamoto, K. Infrared and Raman spectra of inorganic and coordination compounds, 4th ed., Wiley, New York (1986).

[f] Dymek, C. J. et al. Spectral identification of $Al3Cl10^-$ in 1-methyl-3-ethylimidazolium chloroaluminate molten salt. *Polyhedron* **7**, 1139-1145 (1988).

Table 2 Ab initio vibrational frequencies for $[EMImAlCl_4](MgCl_2)_{1,2}$ and $[EMImAl_2Cl_7](MgCl_2)_{1,2}$ in the far infrared region compared to experimental Raman and IR frequencies for $[EMImCl(AlCl_3)_{1.5}](\delta\text{-}MgCl_2)_{0.2}$.

Structure	Calculated frequencies (cm^{-1}) At B3LYP/6-311G**	Experimental frequencies (cm^{-1}) Raman	IR	Assignment[a]
$AlCl_4^-+EMIm^+$+$MgCl_2$ ($AlCl_4^-+EMIm^+$+$2MgCl_2$) ≡ Figure 2c (Figure 2e)	177(172)	180	180	$\delta(AlCl_4^-)$
	193			$\delta(AlCl_4^-)$, $\delta(MgCl_2)$
	(209)	210	210	$\delta(AlCl_4^-)$, $\delta((MgCl_2)_2)$
	237	237		scissoring $AlCl_4^-$next to Mg
	241[b] (240[b])	237		γ(N-Me)
	(245)			$\nu((MgCl_2)_2)$
	(256, 267) Raman inactive		277	$\nu((MgCl_2)_2)$
	(271)		277	$\nu((MgCl_2)_2)$
	342			$\nu_s(MgCl_2)$
	351(343) weak IR, strong Raman	348		$\nu(AlCl_4^-)$
	381[b] IR inactive (383[b])			γ(N-Et)
	(388,392) Raman inactive		385	$\nu((MgCl_2)_2)$
	(419,426,436) Raman inactive		430,447	$\nu(AlCl_4^-)$, $\nu((MgCl_2)_2)$
	428[b] (430[b])	433		r(N-Et), r(N-Me)
	450 Raman inactive		447	$\nu_{as}(AlCl_4^-)$
	511 Raman inactive		499	$\nu_{as}(AlCl_4^-)$, $\nu_{as}(MgCl_2)$
	(522)			$\nu_s(AlCl_4^-)$
	528(606)			$\nu(AlCl_4^-)$
$Al_2Cl_7^-$+ $EMIm^+$+ $MgCl_2$ ($Al_2Cl_7^-+EMIm^+$+$2MgCl_2$) ≡ Figure 2d (Figure 2f)	164(168)	150	150	$\delta(Al_2Cl_7^-)$, $\delta(MgCl_2)$
	179(176)	180	180	$\delta(Al_2Cl_7^-)$, $\delta(MgCl_2)$
	197(201)			$\delta(Al_2Cl_7^-)$, $\delta(MgCl_2)$
	240[b] (239[b])	237		γ(N-Me)
	(247, 253)		277	$\nu(MgCl_2)_2$
	(266) Raman inactive		277	$\nu(MgCl_2)_2$
	(297)	310		$\nu(Al_2Cl_7^-)$,$\nu(MgCl_2)_2$
	320	310		$\nu_s(Al_2Cl_7^-)$ bridge
	328		337	$\nu_s(MgCl_2)$
	347		337	$\nu_{as}(Al_2Cl_7^-)$ bridge
	(347)	348		$\nu(Al_2Cl_7^-)$
	(360)			$\nu((MgCl_2)_2)$
	366[b] (381[b]) IR inactive			γ(N-Et)
	386(389)		385	$\nu(Al_2Cl_7^-)$ termin., out of phase
	439[b] (429[b])	433		r(N-Et), r(N-Me)
	447(447)	433	430	$\nu(Al_2Cl_7^-)$ termin.
	(477, 491) Raman inactive		447,499	$\nu((MgCl_2)_2)$
	(517)			$\nu((MgCl_2)_2)$

	521	528	$\nu(Al_2Cl_7^-)$ termin.
	529	528	$\nu_{as}(MgCl_2)$
	(552)	555	$\nu(Al_2Cl_7^-)$ termin.
	591,609(588,600)		$\nu(Al_2Cl_7^-)$ termin.

[a] ν stretching, δ bending, r rocking, γ out of plane, s symmetrical, as antisymmetrical.
[b] Calculated frequency is not scaled.

EMIm/(AlI_4)(δ-$MgCl_2$)$_{0.023}$

First principles electronic structure calculations were performed using the GAUSSIAN 09 suite of programs.[1] Density functional theory (DFT) with Becke's 3-parameter hybrid functional (B3LYP)[2] was used. The 6-311G** split valence basis set[3] was used for H, C, N, Mg, and a supplemented all electron 6-311G** basis set[4] was used Al. Optimizations were performed over all degrees of freedom without symmetry constraints and tight convergence criteria. Frequency calculations were performed at the same level of theory to confirm the resulting stationary points as local minima. To minimize the effect of systematic errors in calculated vibrational frequencies, all of the computed frequencies were scaled by 1.04 except for the cationic vibrations, which were not scaled. This was similar to the scaling factor used in our previous work on δ-$MgCl_2$ based IL systems[5] and also the scaling factor obtained using the SQM method for organic molecules containing C, H, N, O, S, P, and Cl atoms.[6]

Clusters of $[EMImI_3]^{-2}$, $EMImAlI_4$, and $EMImAl_2I_7$, were optimized using the method described above to study and assign the experimental vibrational IR and Raman spectra of the two ionic liquid systems: EMImI and $EMImAlI_4$. The optimizations were performed beginning from different initial starting configurations. The lowest energy structure was used for further investigation. Monomeric and dimeric magnesium iodide were added to the $EMImAlI_4$ and $EMImAl_2I_7$ clusters in order to investigate the effect of the δ-MgI_2 salt. The vibrational spectra of the resulting clusters were compared to the IR and Raman spectra of $EMImAlI_4$/(δ-MgI_2)$_{0.023}$.

Diffuse functions for hydrogen and heavy atoms, including iodine, were added to the $EMImAlI_4$/MgI_2 and $EMImAl_2I_7$/MgI_2 clusters. It was found that the optimized structures change insignificantly and vibrational frequencies shift by one or two wavenumbers. As the effect of diffuse functions was determined to be negligible for the vibrational analysis, they were not included in the calculations.

Assignment of IR and Raman spectra of pristine $EMImAlI_4$:

Figure 1 shows the optimized structures for the studied imidazolium based ionic liquids. Table 1 and 2 summarize the experimental and calculated vibrational frequencies in the far infrared region. From Table 1 it is clear that the EMImI does not show any characteristic vibrational band in the far IR region. In the Raman spectrum of $EMImAlI_4$, there are two strong peaks at 146 and 140 cm^{-1} which are characteristic of the AlI_4^- and $Al_2I_7^-$ anions,[7-8] respectively. The computed frequencies are summarized in Table 1 and reveal two peaks at 144 and 138 cm^{-1} with strong Raman intensities for $EMImAlI_4$ and $EMImAl_2I_7$ clusters, respectively.

The far IR spectrum of $EMImAlI_4$ shows a strong peak at 242 cm^{-1}. Calculated frequencies for the $EMImAlI_4$ cluster only show an out of plane vibrational mode for the ethyl group at 243 cm^{-1}. This vibrational mode is usually weak (similar to the IR peak of EMImI at 244 cm^{-1}) and cannot explain the strong peak observed at 242 cm^{-1}. The asymmetrical stretching of the Al–I–Al bridge in $EMImAl_2I_7$ cluster appears at 245 cm^{-1} with a high IR intensity which can be related to the strong peak at 242 cm^{-1}.

The peak at 291 cm^{-1} is related to the cation vibrations at 296 and 297 cm^{-1}. However, the IR intensity of this vibrational mode is not high enough to fully describe the observed peak at 291 cm^{-1}. The $EMImAl_2I_7$ cluster shows symmetrical stretching of $Al_2I_7^-$ at 300 cm^{-1} which may be related to the experimentally observed peak at 291 cm^{-1}.

The Raman peak at 146 cm^{-1} is an indication of the presence of the AlI_4^- ionic species and the Raman peak at 140 cm^{-1} and IR peaks at 242 and 291 cm^{-1} indicate the presence of $Al_2I_7^-$. Hence, the pristine IL ($EMImAlI_4$) contains both AlI_4^- and $Al_2I_7^-$ ionic species, rather than only AlI_4^-.

The observed peak at 341 cm^{-1} can only be related to the stretching vibrational mode of AlI_4^- at 331 cm^{-1} in the $EMImAlI_4$ cluster. The peaks at 359 and 374 cm^{-1} are assigned to the stretching modes of both AlI_4^- and $Al_2I_7^-$.

Assignment of IR and Raman spectra of $EMImAlI_4/(\delta\text{-}MgI_2)_{0.023}$:

Addition of δ-MgI_2 to $EMImAlI_4$ increases the ratio of the intensity of the two Raman peaks corresponding to the AlI_4^- and $Al_2I_7^-$ anions (146 cm^{-1}/140 cm^{-1}). At higher concentrations of δ-MgI_2, the ratio of AlI_4^- to $Al_2I_7^-$ increases. The Raman peak at 146 cm^{-1} related to the AlI_4^- anionic species is also blue shifted to 147 cm^{-1} in $EMImAlI_4/(\delta\text{-}MgI_2)_{0.023}$. The same behaviour is observed in the calculated frequencies for the stretching mode of AlI_4^- (shifts from 144 to 146 cm^{-1}) upon addition of MgI_2 to the $EMImAlI_4$ cluster (see Table 2).

In Table 2, both clusters containing $(MgI_2)_2$ species have vibrational modes with high intensity at wavenumbers that are inactive in the experimental IR and Raman spectra (at 268 cm^{-1} for $EMImAlI_4/(MgI_2)_2$ and at 258 and 261 cm^{-1} for $EMImAl_2I_7/(MgI_2)_2$. Similar high intensity bands appear in the vibrational spectra of $EMImAlI_4/(MgI_2)_3$ and $EMImAl_2I_7/(MgI_2)_3$ clusters (result not shown). Hence, the computational frequency analysis disregards the presence of dimeric and trimeric magnesium iodide in the IL system.

The $EMImAl_2I_7/MgI_2$ cluster has vibrational modes regarding the stretching of Mg–I bonds at 210 cm^{-1} with relatively high IR and Raman intensity and also at 260 cm^{-1} with high IR intensity that do not appear in the experimental spectra. Hence, the presence of $EMImAl_2I_7/MgI_2$ species in the $EMImAlI_4/(\delta\text{-}MgI_2)_{0.023}$ system is also ruled out due to the absence of these computed vibrational modes in the experimental IR and Raman spectra.

The peak at 341 cm^{-1} is related to the stretching mode of AlI_4^- and MgI_2 in both $EMImAlI_4$ and $EMImAlI_4/MgI_2$ clusters while the 374 cm^{-1} is assigned to the $EMImAlI_4$ and $EMImAl_2I_7/MgI_2$ and $EMImAlI_4/MgI_2$ clusters. The ratio of the intensity of the two bands of the experimental spectra at 341 and 374 cm^{-1} increases with increasing concentration of δ-MgI_2. This is in agreement with the increase of the $EMImAlI_4$ and $EMImAlI_4/MgI_2$ species upon addition of δ-MgI_2 to the system.

Conclusions:

DFT based electronic structure calculations suggest that the pristine IL, $EMImAlI_4$, contains both AlI_4^- and $Al_2I_7^-$ anionic species. Addition of the buffering δ-MgI_2 salt to the pristine IL results in an increase in the ratio of the AlI_4^- to $Al_2I_7^-$ anions. The added δ-MgI_2 salt is dissolved in the system forming the $EMImAlI_4/MgI_2$ species. It is found that the MgI_2 salt favours interaction with the IL in the form of the monomer rather than either the dimer or trimer.

References:

(1) Frisch, M. J.; Trucks, G. W.; Schlegel, H. B.; Scuseria, G. E.; Robb, M. A.; Cheeseman, J. R.; Scalmani, G.; Barone, V.; Mennucci, B.; Petersson, G. A.; et al., Gaussian 09, Revision A.01. Wallingford CT, 2009.

(2) Becke, A. D., Density-Functional Thermochemistry .3. The Role of Exact Exchange. *J Chem Phys* **1993,** *98*, 5648-5652.

(3) Mclean, A. D.; Chandler, G. S., Contracted Gaussian-Basis Sets for Molecular Calculations .1. 2nd Row Atoms, Z = 11-18. *J Chem Phys* **1980,** *72*, 5639-5648.

(4) Glukhovtsev, M. N.; Pross, A.; Mcgrath, M. P.; Radom, L., Extension of Gaussian-2 (G2) Theory to Bromine-Containing and Iodine-Containing Molecules - Use of Effective Core Potentials. *J Chem Phys* **1995,** *103*, 1878-1885.

(5) Bertasi, F.; Hettige, C.; Sepehr, F.; Bogle, X.; Pagot, G.; Vezzù, K.; Negro, E.; Paddison, S. J.; Greenbaum, S. G.; Vittadello, M.; et al., A Key Concept in Magnesium Secondary Battery Electrolytes. *ChemSusChem* **2015**, in press.

(6) Katsyuba, S.; Vandyukova, E., Scaled quantum mechanical computations of vibrational spectra of organoelement molecules, containing the atoms P, S, and Cl. *Chem Phys Lett* **2003,** *377*, 658-662.

(7) Begun, G. M.; Boston, C. R.; Torsi, G.; Mamantov, G., Raman Spectra of Molten Aluminum Trihalide-Alkali Halide Systems. *Inorg Chem* **1971,** *10*, 886-889.

(8) Manteghetti, A.; Potier, A., Vibrational Spectroscopy and Normal Coordinate Analysis of Mu-Halo Halo Hexahalodialuminates Ions Al_2Cl_7,Al_2Br_7,Al_2I_7 in Some Salts and in Friedel-Crafts Solutions. *Spectrochim Acta A* **1982,** *38*, 141-148.

Table 1. Experimental vibrational spectra of EMImI and $EMImAlI_4$ and calculated vibrational modes for $[EMImI_3]^{-2}$, $EMImAlI_4$, and $EMImAl_2I_7$ clusters in cm^{-1}.

Experiment[a] EMImI		Computation $[EMImI_3]^{-2}$	Assignment[b]	Experiment[a] $EMImAlI_4$		Computation $EMImAlI_4$	Computation $EMImAl_2I_7$	Assignment[b]
IR	Raman	Freq. (I_{IR}, I_{Ra})[c]		IR	Raman	Freq. (I_{IR}, I_{Ra})[c]	Freq. (I_{IR}, I_{Ra})[c]	
						48(0.3, 1.9)	48(0.4, 0.8)	Cat-An
						59(1.4, 2.1)	58(3.9, 1.6)	Cat-An
		66(1.1, 0.8)	Cat-An			68(0.9, 0.1)	65(0.2, 1.2)	Cat-An, tors(N-Et)
		76(7.6, 0.5)	Cat-An			74(7.2, 1.0)	70(6.1, 2.1)	Cat-An
75(s)		77(31.4, 0.7)	Cat-An				73(3.2, 3.8)	Cat-An
							77(1.2, 2.6)	Cat-An, tors(N-Et)
						78(0.5, 2.4)	78(1.2, 1.4)	Cat-An, $\delta(AlI_4^-)$, $\delta(Al_2I_7^-)$
						81(0.6, 2.5)		$\delta(AlI_4^-)$
						89(9.5, 4.5)	89(3.9, 1.2)	$\delta(AlI_4^-)$, $\delta_t(Al_2I_7^-)$, tors(N-Et), tors(N-Me)
							94(0.1,0.9)	$\delta_b(Al_2I_7^-)$, $\delta_t(Al_2I_7^-)$
88(s)		100(4.8, 3.4)	tors(N-Me)			100(0.3, 0.8)	103(0.1, 1.6)	tors(N-Me)
150(w)		132(1.0, 0.5)	γ(N-Et)	146(w)		137(0.9, 4.9)	137(0.6, 4.0)	γ(N-Et)
					140(s)		138(0.3, 18.4)	$\nu^s_b(Al_2I_7^-)$, $\nu^s_t(Al_2I_7^-)$
					146(s)	144(0.3, 10.6)		$\nu(AlI_4^-)$
							146(3.7, 0.7)	$\nu^{as}_b(Al_2I_7^-)$, $\nu^s_t(Al_2I_7^-)$, γ(N-Et)
		201(0.1, 1.4)	tors(C-CH_3)			208(0.2, 0.2)	208(0.4, 0.2)	tors(C-CH_3)
244(w)		234(1.4, 1.4)	γ(N-Me)	230		243(1.9, 1.5)	238(35.0, 1.4)	γ(N-Me)
				242(s)			245(170.5, 1.3)	$\nu^{as}_b(Al_2I_7^-)$, γ(N-Me)
298(w)		296(4.1, 0.7)	δ(N-Me), δ(N-Et)			297(1.5, 0.7)	296(1.8, 0.8)	δ(N-Me), δ(N-Et)
				291(w)			300(26.0, 3.0)	$\nu^s_b(Al_2I_7^-)$
						319(97.3, 0.8)		$\nu(AlI_4^-)$
				341(m)		331(104.1, 1.0)		$\nu(AlI_4^-)$
				359(sh, m)			356(30.5, 0.7)	$\nu^{as}_t(Al_2I_7^-)$
							362(144.4, 0.5)	$\nu_t(Al_2I_7^-)$
				374(vs)		379(141.3, 1.5)	383(103.5, 2.1)	$\nu(AlI_4^-)$, $\nu_t(Al_2I_7^-)$
							392(176.0, 5.0)	$\nu_t(Al_2I_7^-)$
		398(1.2, 2.0)	γ(N-Et)			390(0.2, 3.3)	389(0.2, 3.3)	γ(N-Et)
		426(5.2, 2.4)	r(N-Me), r(N-Et)	424(w)		423(1.3, 1.8)	425(0.8, 2.4)	r(N-Me), r(N-Et)
				443(w)				
595(w)		598(0.5, 2.2)	δ(N1-C2-N3)	594(w)		594(2.5, 3.9)	594(2.4, 3.3)	δ(N1-C2-N3)

[a] Labels in parenthesis are experimental IR and Raman intensities: w, weak; m, medium; s, strong; v, very; sh, shoulder; br, broad.

[b] Labels: ν, stretching; δ, bending; r, rocking; γ, out of plane; tors, torsion; s, symmetrical; as, antisymmetrical; t, terminal; b, bridge; Cat-An, vibrations in which the imidazolium cation oscillates around the anion.

[c] Values in parenthesis are calculated IR intensities (km/mole) and Raman scattering activities ($Å^4$/AMU).

Table 2. Experimental vibrational spectra of $EMImAlI_4/(\delta\text{-}MgI_2)_{0.023}$ and calculated vibrational modes for $EMImAlI_4/MgI_2$, $EMImAlI_4/(MgI_2)_2$, $EMImAl_2I_7/MgI_2$, and $EMImAl_2I_7/(MgI_2)_2$ clusters in cm^{-1}.

Experiment[a]		Computation				Assignment[b]
$EMImAlI_4/(\delta\text{-}MgI_2)_{0.023}$		$EMImAlI_4/MgI_2$	$EMImAlI_4/(MgI_2)_2$	$EMImAl_2I_7/MgI_2$	$EMImAl_2I_7/(MgI_2)_2$	
IR	Raman	Freq. (I_{IR}, I_{Ra})[c]	Freq. (I_{IR}, I_{Ra})[c]	Freq. (I_{IR}, I_{Ra})[c]	Freq. (I_{IR}, I_{Ra})[c]	
					47(0.5, 0.4)	tors(N-Et)
		49(0.8, 1.0)	47(0.1, 2.2)	47(1.7, 1.8)		Cat-An
			53(0.4, 1.4)	53(0.4, 1.2)	50(0.4, 0.9)	Cat-An
		56(0.8, 0.4)	56(0.8, 1.2)	55(0.6, 0.4)	55(0.3, 0.8)	Cat-An, r($(MgI_2)_2$)
		59(5.0, 1.8)	60(2.8, 0.3)	60(1.7, 1.1)	59(0.6, 2.9)	Cat-An
			67(0.8, 0.6)	65(3.2, 2.3)	64(3.1, 2.1)	Cat-An
					67(1.6, 0.8)	Cat-An
		75(4.9, 2.2)	72(1.7, 1.3)	72(5.0, 0.7)		Cat-An
			77(0.3, 1.6)	78(0.5, 1.6)	76(1.1, 3.0)	$\delta(AlI_4^-)$, $\delta(Al_2I_7^-)$
					77(21.5, 1.3)	Cat-An
			79(0.0, 2.1)			$\delta(AlI_4^-)$
			79(21.7, 2.7)			Cat-An
		80(1.7, 1.4)				Cat-An, $\delta(AlI_4^-)$, $\delta(MgI_2)$
				84(0.7, 1.5)	83(4.0, 3.4)	$\delta(Al_2I_7^-)$, $\delta(MgI_2)$, tors(N-Me)
					86(1.3, 0.6)	$\delta_t(Al_2I_7^-)$
		89(1.8, 3.1)				Cat-An, $\delta(AlI_4^-)$, $\delta(MgI_2)$
			93(0.0, 4.1)			$\delta(AlI_4^-)$, $\delta((MgI_2)_2)$, tors(N-Me)
				93(1.4, 2.5)		$\delta(Al_2I_7^-)$, $\delta(MgI_2)$, tors(N-Me)
			93(2.8, 1.4)	98(0.7, 1.5)	94(0.2, 0.6)	tors(N-Me)
					96(0.0, 0.5)	$\delta(Al_2I_7^-)$, $\delta((MgI_2)_2)$
				100(2.4, 2.1)		$\delta(Al_2I_7^-)$, $\delta(MgI_2)$, tors(N-Me)
		106(6.5, 2.0)	109(0.5, 2.0)			$\delta(AlI_4^-)$, $\nu(MgI_2)$, $\nu((MgI_2)_2)$
					107(0.6, 0.9)	$\nu((MgI_2)_2)$
			120(1.5, 3.4)		115(1.8, 6.9)	$\delta(AlI_4^-)$, $\nu((MgI_2)_2)$
		129(2.5, 0.7)				tors(N-Me)
		133(8.1, 0.8)				ν(Mg-I-Al), tors(N-Me), γ(N-Et)
				139(0.5, 15.9)	138(0.1, 16.1)	$\nu^s_b(Al_2I_7^-)$, $\nu^s_t(Al_2I_7^-)$, ν(Mg-I)
	140(m)					$\nu^s_b(Al_2I_7^-)$, $\nu^s_t(Al_2I_7^-)$ from $EMImAl_2I_7$
			144(0.7, 3.8)	140(1.7, 0.8)	143(1.8, 4.9)	γ(N-Et)
				143(1.3, 1.6)		ν(Mg-I-Al)
					145(4.3, 0.4)	$\nu^{as}_b(Al_2I_7^-)$, $\nu^s_t(Al_2I_7^-)$
146(w)		145(0.2, 2.4)				tors(N-Me), γ(N-Et)
	147(s)	146(0.7, 10.9)	144(3.3, 13.6)			$\nu(AlI_4^-)$

Experiment[a]		Computation				Assignment[b]
$EMImAlI_4/(\delta\text{-}MgI_2)_{0.023}$		$EMImAlI_4/MgI_2$	$EMImAlI_4/(MgI_2)_2$	$EMImAl_2I_7/MgI_2$	$EMImAl_2I_7/(MgI_2)_2$	
IR	Raman	Freq. (I_{IR}, I_{Ra})[c]	Freq. (I_{IR}, I_{Ra})[c]	Freq. (I_{IR}, I_{Ra})[c]	Freq. (I_{IR}, I_{Ra})[c]	
				153(21.9, 2.6)		ν(Mg-I)
			185(9.7, 1.0)		184(7.0, 0.7)	$\nu((MgI_2)_2)$
			189(1.1, 0.2)			ν(Mg-I-Al)
					206(0.1, 0.4)	$\nu_t(Al_2I_7^-)$, ν(Mg-I)
				210(106.0, 8.3)		$\nu(MgI_2)$
		212(0.1, 0.2)	214(1.0, 0.7)	207(0.4, 0.2)	207(0.2, 0.2)	tors(C-CH_3)
229(m, b)		235(125.1, 4.4)				$\nu(MgI_2)$
242(s)						$\nu^{as}{}_b(Al_2I_7^-)$ from $EMImAl_2I_7$
242(s)		242(3.2, 1.6)	241(1.4, 2.4)	237(2.8, 1.6)	238(2.6, 2.0)	γ(N-Me)
				260(179.2, 0.5)	258(192.3, 0.0)	$\nu^{as}{}_b(Al_2I_7^-)$, ν(Mg-I)
			268 (365.1, 1.4)		261(422.8, 3.5)	$\nu((MgI_2)_2)$
			284(64.8, 0.0)		284(28.1, 0.6)	$\nu((MgI_2)_2)$
			293(35.2, 0.0)			ν(Mg-I), ν(Al-I)
					294(22.7, 1.3)	$\nu((MgI_2)_2)$, $\nu_t(Al_2I_7^-)$
			301(115.1, 0.3)		301(44.1, 1.2)	$\nu(AlI_4^-)$, $\nu^s{}_b(Al_2I_7^-)$, ν(Mg-I)
					301(63.9, 0.5)	$\nu^s{}_b(Al_2I_7^-)$, ν(Mg-I)
291(w)		296(18.4, 0.3)	294(2.0, 0.2)	295(1.1, 0.6)	294(0.4, 1.0)	δ(N-Me), δ(N-Et)
312(sh, vw)		308(58.3, 0.3)				δ(N-Me), δ(N-Et), ν(Mg-I-Al)
			308(105.3, 0.2)			$\nu((MgI_2)_2)$, ν(Al-I)
				309(48.6, 2.2)		$\nu^s{}_b(Al_2I_7^-)$
				339(46.0, 0.8)	340(150.2, 1.2)	$\nu_t(Al_2I_7^-)$
				347(151.8, 2.4)	343(39.3, 3.5)	$\nu_t(Al_2I_7^-)$
341(sh, m)		344(110.5, 1.1)	351(65.8, 1.8)			$\nu(AlI_4^-)$, ν(Mg-I)
360(sh, m)		362(91.7, 1.3)		373(90.1, 1.5)		$\nu^{as}(MgI_2)$
		390(0.7, 2.7)	380(0.3, 3.4)	378(1.2, 1.5)	376(0.2, 4.8)	γ(N-Et)
				392(87.8, 2.6)		$\nu_t(Al_2I_7^-)$, γ(N-Et)
374(vs)		392(146.9, 1.8)				$\nu(AlI_4^-)$, $\nu(MgI_2)$
			406(116.7, 2.4)			$\nu(AlI_4^-)$
				406(170.1, 4.1)	411(159.4, 1.2)	$\nu_t(Al_2I_7^-)$
					413(75.0, 4.6)	$\nu_t(Al_2I_7^-)$
424(w)		424(1.6, 1.2)	430(1.0, 0.9)	431(0.7, 2.3)	434(1.0, 2.1)	r(N-Me), r(N-Et)
443(w)						
593(w)		596(2.7, 3.8)	598(0.1, 5.1)	595(2.1, 2.5)	596(7.7, 6.8)	δ(N1-C2-N3)

[a] Labels in parenthesis are experimental IR and Raman intensities: w, weak; m, medium; s, strong; v, very; sh, shoulder; br, broad.

[b] Labels: ν, stretching; δ, bending; r, rocking; γ, out of plane; tors, torsion; s, symmetrical; as, antisymmetrical; t, terminal; b, bridge; Cat-An, vibrations in which the imidazolium cation oscillates around the anion.

[c] Values in parenthesis are calculated IR intensities (km/mole) and Raman scattering activities ($Å^4$/AMU).

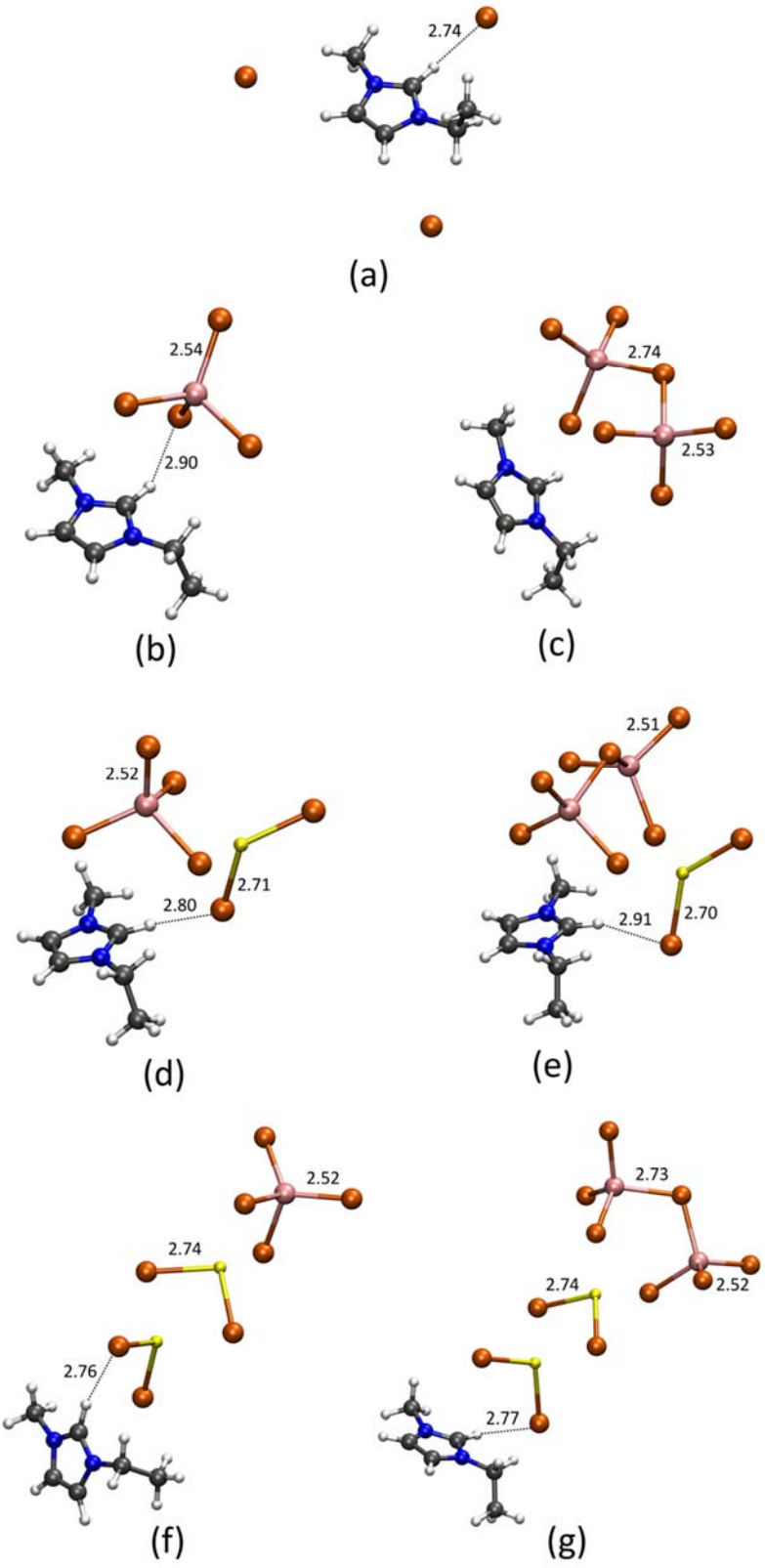

Figure 1. Optimized geometries of the ionic liquid complexes determined at the B3LYP/6-311G** level of theory. (a) Structure of $[EMImI_3]^{-2}$; (b) Structure of $EMImAlI_4$; (c) Structure of $EMImAl_2I_7$; (d) Structure of $EMImAlI_4$ moiety with MgI_2; (e) Structure of $EMImAl_2I_7$ moiety with MgI_2; (f) Structure of $EMImAlI_4$ moiety with $(MgI_2)_2$; (g) Structure of $EMImAl_2I_7$ moiety with $(MgI_2)_2$. Colour code: iodine, orange; aluminium, pink; magnesium, yellow; carbon, grey; nitrogen, blue; hydrogen, white. Distances between iodine and hydrogen are only shown where less than 3 Å.